Proceedings of AVT-200 Specialists' Meeting on Hypersonic Laminar-Turbulent Transition, San Diego, CA. April 16-19, 2012.

Optical Detection of Transitional Phenomena on Slender Bodies in Hypervelocity Flow

N. J. Parziale, J. S. Jewell, H. G. Hornung, J. E. Shepherd
California Institute of Technology
1200 E. California Blvd. MC 205 45
Pasadena, CA 91125
USA

nick.parziale@gmail.com

ABSTRACT

Measurement of the phenomena associated with hypervelocity boundary layer transition requires the development of high-speed detection techniques. Two reasons for the current search for a reliable non-intrusive optical technique include: 1) high-enthalpy facilities suffer from a harsh environment in the test section after the test time, 2) optical diagnostics tend to achieve higher sampling rates than direct mechanical measurement. Two approaches utilizing optical detection are described in this work: temperature measurement by spontaneous emission and laser differential interferometry. A model for the detection of spontaneous emission from a seed gas is formulated, which enables the measurement of spatially-averaged temperature in the boundary layer. This model is applied to data taken during three experiments in a free-piston reflected shock tunnel. The results indicate that the technique may be used to track turbulent bursts in a hypervelocity boundary layer; however, the spontaneous emission technique ultimately falls short of the goal of tracking linear wave packets. Furthermore, the uncertainty in the results from the spontaneous emission experiments is large. Full-field laser differential interferometry is implemented. Preliminary results indicate the ability to track turbulent precursors.

1.0 INTRODUCTION

The instability mechanism in hypersonic flow over cold-wall slender bodies is acoustic in nature; acoustic waves become trapped in a wave guide comprised of the body wall and the sonic line in the boundary layer [1–4]. Numerous investigations of flow over a slender cone in high-enthalpy facilities have been performed [5–8]; yet, detailed measurements of the character of the disturbances formed as a result of this acoustic wave guide have not been made. Data from cold hypersonic facilities (reservoir enthalpy: $h_R < 2$ MJ/kg) indicate that the most strongly amplified frequency of the acoustic instability is typically below 500 kHz [3, 9, 10]. In high-enthalpy facilities (mass specific reservoir enthalpy: $h_R =$ 5-20 MJ/kg), the velocity at the edge of the boundary layer is considerably higher, so that the most strongly amplified acoustic mode frequency on a slender cone is also higher, $\sim$1-3 MHz [6, 7, 11]. These time scales eliminate piezo-electric pressure transducers, surface heat transfer gauges, and hot wire anemometry techniques as candidates for measuring the acoustic instability at conditions typical of an experiment in a high-enthalpy facility, due to inadequate temporal resolution.

This work describes the development of two techniques for the optical measurement of transitional boundary layer phenomena. One method introduces trace amounts of a seed gas with a strong oscillator strength (namely, lithium for its D1 and D2 spectral lines) into the test gas and tracking the spontaneous emission of the seed gas from the boundary layer; the rate of spontaneous emission is related to the temperature of the gas and, thus, indicates temperature transients. A second method of optical detection of transitional phenomena is also presented, high speed differential interferometry.

2.0 FACILITY

All experiments are performed in T5, the reflected shock tunnel at the California Institute of Technology (Figure 1). This facility is designed designed to simulate high-enthalpy real gas effects on the aerodynamics of vehicles flying at high speed through the atmosphere. Unlike conventional cold flow facilities, the free-piston driven reflected shock tunnel generates high Mach number flows by increasing the velocity, not decreasing the speed of sound.

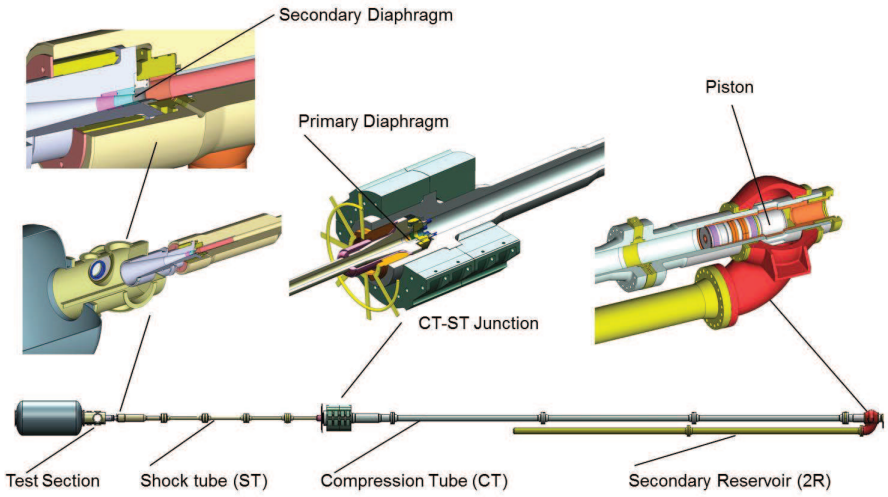

Figure 1: A schematic of T5, with a blown up view of each of the major sections.

An experiment is conducted as follows: a 120 kg aluminum piston is loaded into the compression tube/secondary reservoir junction. A thin mylar secondary diaphragm is inserted at the nozzle throat at the end of the shock tube adjoining the test section, and a primary diaphragm (stainless steel, 7 mm thick) is inserted at the compression tube/shock tube junction. The test section, shock tube and compression tube are taken to vacuum. The shock tube is filled with the test gas, N_2 in the present study, to $\sim$85 kPa. The compression tube is filled with a He/Ar mixture to $\sim$100 kPa and the secondary reservoir is filled with air to $\sim$10 MPa. The air in the secondary reservoir is released, driving the piston into the compression tube. This piston motion adiabatically compresses the driver gas of the shock tunnel to the rupture pressure of the primary diaphragm ($\sim$100 MPa). Following the primary diaphragm rupture, a shock wave propagates into the shock tube, is reflected off the end wall, breaks the secondary diaphragm, and re-processes the test gas. The test gas is then expanded through a converging-diverging contoured nozzle to Mach$\approx$5.5 in the test section.

3.0 SPONTANEOUS EMISSION DETECTION

This method entails introducing trace amounts of a seed gas with a strong line-strength (vaporized lithium, in this case) to the test gas, and focusing the spontaneous emission from a point of interest onto a fiber-coupled photodetector (Figure 2). Typically in fluid dynamics work, the light emission is stimulated to produce a measurand, as in [12–16]. Due to the high temperatures and densities available in T5, it is possible to detect the spontaneous emission from the seed gas. We show that spontaneous emission can be used as an indicator of local temperature, and fluctuations associated with boundary layer transition on a slender body at high speed. A model relating the local temperature of the gas to the emissive power of the gas (measured by the photodetector) and the edge pressure on the cone (calculated from the run conditions) is developed, and data from three experiments are presented.

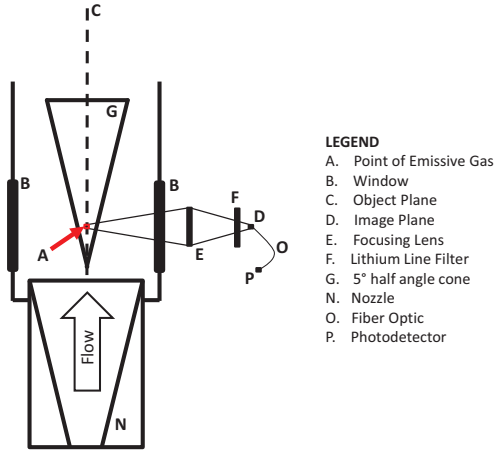

Figure 2: Schematic of the optical setup for the detection of the spontaneous emission of lithium.

3.1 Spontaneous Emission Model

In this section, a model for the emissive power of a heated gas is formulated following the development in [17]. In its ground state, lithium has the electronic configuration: $1s^2\ 2s^1$, and in its first excited state has the electron configuration: $1s^2\ 2s^0\ 2p^1$. The term symbol for the ground state is ${}^2S_{1/2}$; the first electronically excited state is split and has the term symbols: ${}^2P_{1/2}$ and ${}^2P_{3/2}$ [18–20]. Let the population density of each state be: $N_{{}^2S_{1/2}}$, $N_{{}^2P_{3/2}}$ and $N_{{}^2P_{1/2}}$. The rate constants for absorption are $\mathbf{b}_{{}^2S_{1/2}:{}^2P_{3/2}}$ and $\mathbf{b}_{{}^2S_{1/2}:{}^2P_{1/2}}$; the rate constants for stimulated emission are $\mathbf{b}_{{}^2P_{3/2}:{}^2S_{1/2}}$ and $\mathbf{b}_{{}^2P_{1/2}:{}^2S_{1/2}}$. The spontaneous emission rate constants are the Einstein A coefficients: $\mathbf{A}_{{}^2P_{3/2}:{}^2S_{1/2}}$ and $\mathbf{A}_{{}^2P_{1/2}:{}^2S_{1/2}}$. The collisional quenching rate constants are: $\mathbf{Q}_{{}^2P_{3/2}:{}^2S_{1/2}}$ and $\mathbf{Q}_{{}^2P_{1/2}:{}^2S_{1/2}}$. The excitation rate constants are: $\mathbf{Q}_{{}^2S_{1/2}:{}^2P_{3/2}}$ and $\mathbf{Q}_{{}^2S_{1/2}:{}^2P_{1/2}}$. The energies associated with photo-ionization are quite high relative to the conditions in T5, so this process is not included in the current model. The relevant processes are shown connecting the ground state to the excited states in Figure 3. The spontaneously emissive power from the first split excited state of lithium is,

$$P_{Spontaneous} = F_G V \frac{\Omega}{4\pi}\left(h\nu_{{}^2P_{3/2}} N_{{}^2P_{3/2}} \mathbf{A}_{{}^2P_{3/2}} + h\nu_{{}^2P_{1/2}} N_{{}^2P_{1/2}} \mathbf{A}_{{}^2P_{1/2}}\right), \quad (1)$$

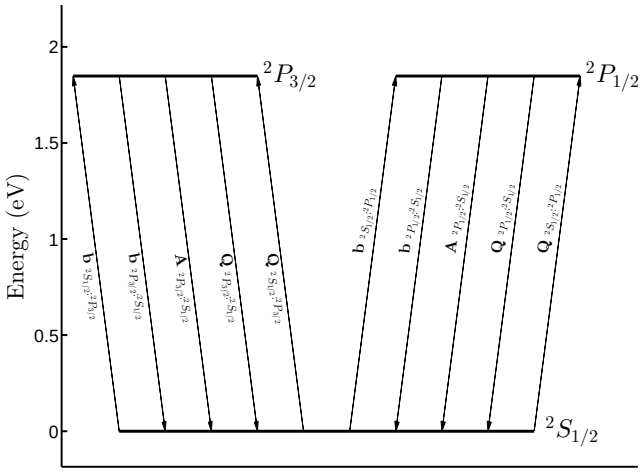

Figure 3: Two-level energy diagram illustrating the relevant processes of excitation and de-excitation of the split first excited state of Lithium.

where, h is Planck's constant, and $\nu_{^2P_{3/2}}$ and $\nu_{^2P_{1/2}}$ are the frequencies of the emitted light. V is the volume of luminous gas, F_G is the correction factor attributed to non-ideal transmission through glass, and Ω is the collection solid angle. We are considering only spontaneous emission, so that $\mathbf{b}_{^2S_{1/2}:^2P_{3/2}}$, $\mathbf{b}_{^2S_{1/2}:^2P_{1/2}}$,$\mathbf{b}_{^2P_{3/2}:^2S_{1/2}}$ and $\mathbf{b}_{^2P_{1/2}:^2S_{1/2}}$ are zero, and the rate equation for the population density of each state is given by

$$\frac{dN_{^2S_{1/2}}}{dt} = -N_{^2S_{1/2}}\mathbf{Q}_{^2S_{1/2}:^2P_{3/2}} - N_{^2S_{1/2}}\mathbf{Q}_{^2S_{1/2}:^2P_{1/2}} + N_{^2P_{3/2}}(\mathbf{A}_{^2P_{3/2}:^2S_{1/2}} + \mathbf{Q}_{^2P_{3/2}:^2S_{1/2}}) + N_{^2P_{1/2}}(\mathbf{A}_{^2P_{1/2}:^2S_{1/2}} + \mathbf{Q}_{^2P_{1/2}:^2S_{1/2}}), \tag{2}$$

$$\frac{dN_{^2P_{3/2}}}{dt} = N_{^2S_{1/2}}\mathbf{Q}_{^2S_{1/2}:^2P_{3/2}} - N_{^2P_{3/2}}(\mathbf{A}_{^2P_{3/2}:^2S_{1/2}} + \mathbf{Q}_{^2P_{3/2}:^2S_{1/2}}) \tag{3}$$

and

$$\frac{dN_{^2P_{1/2}}}{dt} = N_{^2S_{1/2}}\mathbf{Q}_{^2S_{1/2}:^2P_{1/2}} - N_{^2P_{1/2}}(\mathbf{A}_{^2P_{1/2}:^2S_{1/2}} + \mathbf{Q}_{^2P_{1/2}:^2S_{1/2}}). \tag{4}$$

Adding Equations 2, 3 and 4 yields

$$\frac{dN_{^2S_{1/2}}}{dt} + \frac{dN_{^2P_{3/2}}}{dt} + \frac{dN_{^2P_{1/2}}}{dt} = \frac{d}{dt}\left(N_{^2S_{1/2}} + N_{^2P_{3/2}} + N_{^2P_{1/2}}\right) = 0. \tag{5}$$

This result leads to

$$N_{^2S_{1/2}} + N_{^2P_{3/2}} + N_{^2P_{1/2}} = N_0, \tag{6}$$

where N_0 is the total population of lithium atoms, assuming only the first split excited state can be excited at conditions in T5. The values for the $\mathbf{A}_{^2P_{3/2}:^2S_{1/2}}$ and $\mathbf{A}_{^2P_{1/2}:^2S_{1/2}}$, are found in [20–22]. Following [17] and [23], the quenching rate constants are

$$\mathbf{Q}_{a:b} = \sum n_i \sigma_i v_i, \tag{7}$$

where

$$v_i = \left(\frac{8k_bT}{\pi\mu}\right)^{1/2}, \tag{8}$$

n_i is the number density of the de-activating species, σ_i is the cross section for the quenching species i, μ is the reduced mass of the colliding species, k_b is Boltzmann's constant, and v_i is the relative velocity. The deactivating species is assumed to be only N_2, the test gas in the current experiment. This is a good assumption, as the mass fraction of N in the free-stream is less than 0.6 $\%$ for the current shot series. The cross sections used in the calculations are tabulated in [24–26].

The excitation rate constants are calculated by assuming fast electronic-vibrational energy transfer between Li and N_2; this results in the electronic excitation temperature of Li always equaling the vibrational temperature of N_2. According to [27–29], the conversion of translational energy to electron excitation energy is improbable. Atoms are relatively massive and slow-moving compared to the electrons being excited. Particularly on p. 230 of [27], "On the Landau-Teller principle, energy transfer is unlikely when the duration of a collision is much greater than the period of the oscillation being excited. The duration of a collision between atoms is usually taken as 10^{-13} seconds, while the frequency corresponding to electronic transitions is around $5 * 10^{14}$ per second."This thought process was utilized in a technique called line reversal where researchers typically used trace amounts of Na to track the vibrational temperature of a shock heated gas in nonequilibirum gasdynamic studies [27, 28]. They state that the likely process of electronically exciting Na is

$$\mathrm{Na}(^2S) + \mathrm{N_2}(v'' = 7, 8) \rightarrow \mathrm{Na}(^2P) + \mathrm{N_2}(v'' = 0), \tag{9}$$

where seven or eight vibrational quanta from the N_2 are transferred to the Na. The process is likely similar in lithium,

$$\mathrm{Li}(^2S) + \mathrm{N_2}(v'' = 6, 7) \rightarrow \mathrm{Li}(^2P) + \mathrm{N_2}(v'' = 0), \tag{10}$$

where six or seven vibrational quanta from the N_2 are transferred into the Li. Thus, the effective excitation time of the lithium is assumed to be equal to the vibrational relaxation time of N_2, because of this near-resonant relationship [25, 26, 28, 30, 31]. The vibrational relaxation time of N_2 is calculated with a simplified form of the Landau-Teller model,

$$\tau_{\mathrm{N_2}} = \frac{C\exp(K_2/T)^{1/3}}{p_{edge}}, \tag{11}$$

where C and K_2 are tabulated constants and p_{edge} is the pressure at the edge of the boundary layer [32–34]. MATLAB's built in function, **ode15s** (a turn-key stiff IVP solver), is used to compute the numerical solutions to the coupled differential Equations 2, 3 and 4 (Figure 4(a) and Figure 4(b)). These solutions are presented in terms lithium atom fraction. The calculations indicate that the response time is on the order of the fastest rate (quenching) and the number of excited atoms is dependent on the slowest rate (vibrational excitation).
For long times relative to the quenching process (of order 10 ns) the population densities will reach a steady state, that is,

$$\frac{dN_{2S_{1/2}}}{dt} = \frac{dN_{2P_{3/2}}}{dt} = \frac{dN_{2P_{1/2}}}{dt} = 0. \tag{12}$$

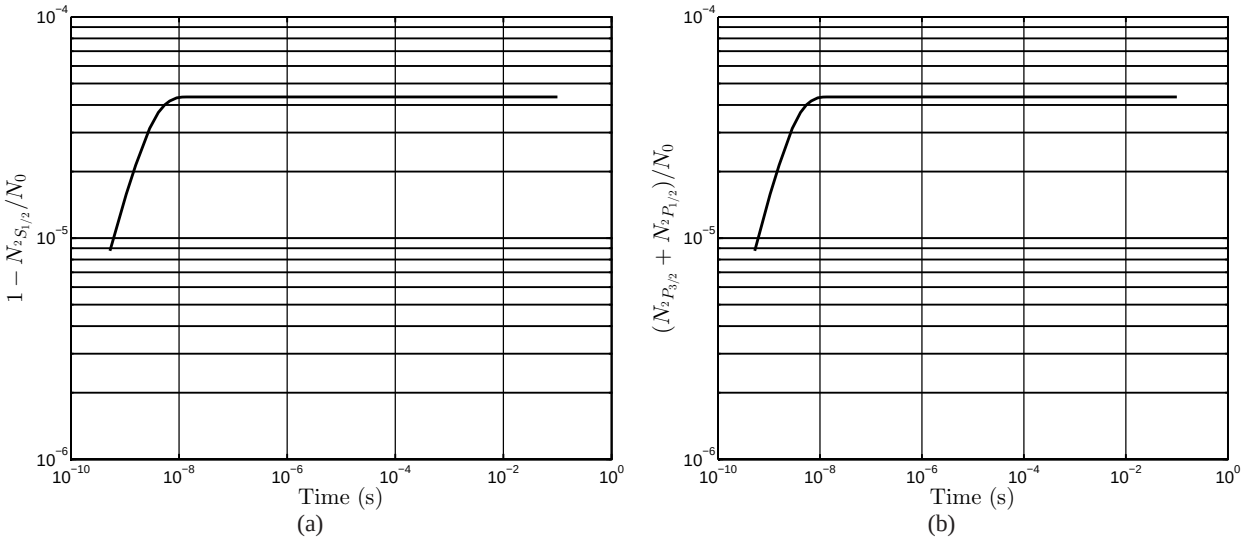

Figure 4: The lower electronic state is seen to decline in (a), and the first split electronic state shows growth in population in (b). These solutions are presented in terms of fraction of Lithium atoms. The calculations indicate that the response time is on the order of the fastest rate (quenching) and the number of excited atoms is dependent on the slowest rate (vibrational excitation).

To find the steady state, population densities of the upper states can be calculated by assuming collisional excitation is balanced by spontaneous emission and collisional quenching,

$$N_{^2P_{3/2}} = \frac{N_{^2S_{1/2}} \mathbf{Q}_{^2S_{1/2}:^2P_{3/2}}}{(\mathbf{A}_{^2P_{3/2}:^2S_{1/2}} + \mathbf{Q}_{^2P_{3/2}:^2S_{1/2}})}, \tag{13}$$

and

$$N_{^2P_{1/2}} = \frac{N_{^2S_{1/2}} \mathbf{Q}_{^2S_{1/2}:^2P_{1/2}}}{(\mathbf{A}_{^2P_{1/2}:^2S_{1/2}} + \mathbf{Q}_{^2P_{1/2}:^2S_{1/2}})}. \tag{14}$$

The population of $N_{^2S_{1/2}}$ can be eliminated algebraically from Equations 13 and 14 with Equations 2, 3, 4, 6 and 12. Substituting the population number densities ($N_{^2P_{3/2}}$ and $N_{^2P_{1/2}}$) into Equation 1 gives,

$$P_{Spontaneous} = F_G h N_0 V \frac{\Omega}{4\pi} \frac{C_1 + C_2}{C_3 + C_4 + C_5 + C_6}, \tag{15}$$

where

$$C_1 = \nu_{^2P_{1/2}:^2S_{1/2}} \left(\mathbf{A}_{^2P_{1/2}:^2S_{1/2}} \mathbf{A}_{^2P_{3/2}:^2S_{1/2}} \mathbf{Q}_{^2S_{1/2}:^2P_{1/2}} + \mathbf{A}_{^2P_{1/2}:^2S_{1/2}} \mathbf{Q}_{^2S_{1/2}:^2P_{3/2}} \mathbf{Q}_{^2S_{1/2}:^2P_{3/2}} \right), \tag{16a}$$

$$C_2 = \nu_{^2P_{3/2}:^2S_{1/2}} \left(\mathbf{A}_{^2P_{1/2}:^2S_{1/2}} \mathbf{A}_{^2P_{3/2}:^2S_{1/2}} \mathbf{Q}_{^2S_{1/2}:^2P_{3/2}} + \mathbf{A}_{^2P_{3/2}:^2S_{1/2}} \mathbf{Q}_{^2S_{1/2}:^2P_{3/2}} \mathbf{Q}_{^2P_{1/2}:^2S_{1/2}} \right), \tag{16b}$$

$$C_3 = \mathbf{A}_{^2P_{1/2}:^2S_{1/2}} \mathbf{A}_{^2P_{3/2}:^2S_{1/2}} + \mathbf{A}_{^2P_{3/2}:^2S_{1/2}} \mathbf{Q}_{^2S_{1/2}:^2P_{1/2}}, \tag{16c}$$

$$C_4 = \mathbf{Q}_{^2S_{1/2}:^2P_{3/2}} \mathbf{Q}_{^2P_{1/2}:^2S_{1/2}} + \mathbf{A}_{^2P_{1/2}:^2S_{1/2}} \mathbf{Q}_{^2P_{3/2}:^2S_{1/2}}, \tag{16d}$$

$$C_5 = \mathbf{Q}_{^2S_{1/2}:^2P_{1/2}} \mathbf{Q}_{^2P_{3/2}:^2S_{1/2}} + \mathbf{Q}_{^2P_{1/2}:^2S_{1/2}} \mathbf{Q}_{^2P_{3/2}:^2S_{1/2}}, \tag{16e}$$

$$C_6 = \mathbf{A}_{^2P_{1/2}:^2S_{1/2}} \mathbf{Q}_{^2S_{1/2}:^2P_{3/2}} + \mathbf{A}_{^2P_{3/2}:^2S_{1/2}} \mathbf{Q}_{^2P_{1/2}:^2S_{1/2}}. \tag{16f}$$

The luminous volume, V, is assumed to be $V = L_{view}\pi d_{view}^2/4$; $d_{view} = 1$ mm in diameter and $L_{view} = 10$ mm depth of focus. N_0 is calculated by assuming that all the Li (750 mg) is vaporized, is evenly distributed in the test slug, and is evenly distributed over the viewing diameter, d_{view}. The solid angle is calculated by considering the geometry of the optical setup. The factor, F_G, due to non-ideal light transmission through the lens, window, and band pass filter is $92.5\%\times92.5\%\times57.5\%$, referring to the beam path in Figure 2. The lens and window are made of uncoated BK7 glass, and the Li line filter is an interference filter (ThorLabs FB670-10). The spontaneous emissive power is converted into a potential, V_{out}, by a photodetector. This relation is expressed as

$$V_{out} = \mathcal{R}MGP_{Spontaneous}, \tag{17}$$

where $\mathcal{R}$ is the responsivity of the photodetector, M is the factor gain from avalanche multiplication, and G is the transimpedance gain from the avalanche detector.

3.2 Spontaneous Emission Experiments

A spontaneous emission detector was constructed for a series of three shots to investigate its usefulness as a detector of transitional phenomena, (conditions found in Table 1, computed by the codes ESTC and NENZF [35, 36]). The primary components that make up this emission detector are the focusing lens, the fiber and the photodetector (see Figure 2). The probe point of interest is the boundary layer on a 5 degree half angle cone, 638 mm from the tip. A 250 mm focal-length lens, located 500 mm from the desired probe volume and 500 mm from the 1 mm diameter fiber optic yields a magnification of $1\times$ in the object plane. The photodetector in this study is an amplified avalanche photodetector (ThorLabs APD110A), which outputs an analog voltage to be digitized by a 14-bit Ethernet oscilloscope at 100 MHz (Cleverscope CS328A-XSE).

Parameter	h_R (MJ/kg)	P_R (MPa)	T_∞ (K)	P_∞ (kPa)	ρ_∞ (kg/m^3)	U_∞ (m/s)	Re_∞^{unit} (1/m)
Shot 2666	8.61	72.6	1220	38.2	0.106	3820	1.11E+07
Shot 2667	10.3	52.2	1480	28.7	0.065	4150	6.47E+06
Shot 2668	10.5	51.8	1510	28.7	0.064	4190	6.25E+06

Table 1: Free-stream conditions table for the spontaneous emission experiments. h_R and P_R are the reservoir enthalpy and pressure. T_∞, P_∞, ρ_∞, and U_∞ are the free-stream temperature, pressure, density, and velocity. Re_∞^{unit} is the unit Reynolds number based on the free-stream conditions.

A summary of the results from the experiments (Table 2), indicates that the measured temperature, $T_{Optical}$, calculated from run conditions plugged into Equation 15, differs from the calculated wall normal spatial average temperature, T_{BL-Avg}, by less than 10%. The wall normal spatial average, T_{BL-Avg}, is the average temperature of the boundary layer, calculated from the transformed similarity solution, assuming a power law approximation for the viscosity-temperature relation [37, 38]. This average must be weighted by the circular aperture of the fiber as,

$$T_{BL-Avg} = \frac{1}{A_{probe}} \int_{-r_f}^{r_f} \int_{r_f-\sqrt{r_f^2-x.^2}}^{r_f+\sqrt{r_f^2-x.^2}} T(y)dydx, \tag{18}$$

where r_f is the radius of the fiber and $A_{probe} = \pi r_f^2$. It is advantageous to think about T_{BL-Avg} graphically (Figure 5), particularly how the boundary layer state will influence the measurement. The outline of the fiber in the object plane of the optical system is plotted in black. The laminar boundary layer temperature profile (calculated) is plotted in blue and a perturbation from this laminar profile is sketched in red. This sketch is

made emphasizing the typical flattening out of the boundary layer profile due to transition; however, it should be noted that when a turbulent spot passes over the probed region, the temperature profile will be fluctuating with time. This fluctuating behavior of the transitional boundary layer profile is illustrated nicely in the figures of [39].

Parameter	U_{Edge} (m/s)	P_{Edge} (kPa)	T_{Edge} (K)	T_{BL-Avg} (K)	T_{Eckert} (K)	$T_{Optical}$ (K)	std($T_{Optical}$) (K)
Shot 2666	3790	55.3	1340	1780	2230	1900	65
Shot 2667	4100	41.1	1610	2160	2640	2220	26
Shot 2668	4140	41.1	1650	2220	2690	2100	36

Table 2: Boundary layer conditions table for the spontaneous emission experiments. U_{Edge}, P_{Edge}, and T_{Edge} are the velocity, pressure and temperature at the edge of the boundary layer calculated from a Taylor-Maccoll solution. h_R and P_R are the reservoir enthalpy and pressure. T_{BL-Avg} is the wall normal spatial average temperature in the boundary layer calculated from the similarity solution. T_{Eckert} is the Eckert reference temperature. $T_{Optical}$ is the temperature calculated by using Equation 15 (the response in Figure 6, top)

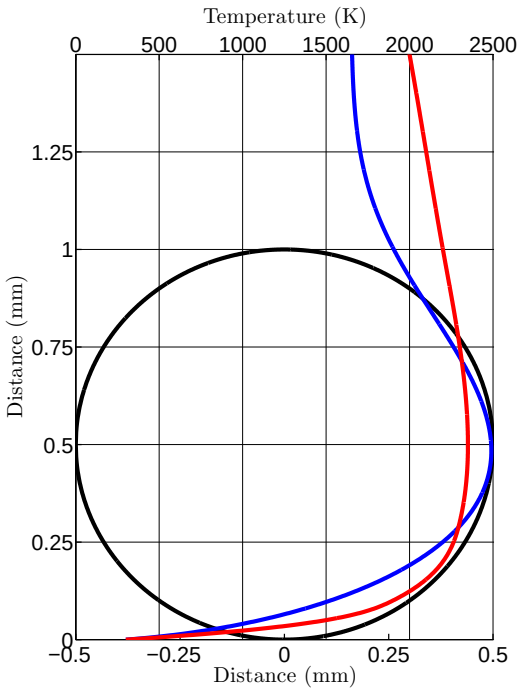

Figure 5: The laminar boundary layer temperature profile (blue, calculated from the similarity solution), and the position of the image of the fiber (black) are overlaid to clearly present what is integrated in Equation 18. This calculation is performed for the conditions in shot 2668. A perturbation to this base state (laminar boundary layer temperature profile) is sketched in red. This qualitatively represents how transitional phenomena perturb the measured temperature, T_{BL-Avg}.

The response of the photodetection technique during shot 2668 (Figure 6, top) shows a signal that varies slightly with time (standard deviation of 36 K with a spatial and temporal average of 2100 K). Between 1850 and 1925 μs of the test time (Figure 6, middle), there is a burst of response (highlighted in green); the spectral

response (Figure 6, bottom) during the green time-window has broad-band response and is high relative to the spectral response of the time-window highlighted in blue. This difference in response is characteristic of a turbulent spot. Note that the measured temperature, $T_{Optical}$, compares favorably to the calculated spatially averaged boundary layer temperature, T_{BL-Avg}.

The repeatability of the technique seems to be fair, comparing shots 2667 and 2668 (these two shots have nearly the same conditions). Shot 2668 was slightly hotter than shot 2667 (the T_{BL-Avg} was 5% higher); however $T_{Optical}$ differed from T_{BL-Avg} in the opposite manner, with $T_{Optical}$ being higher on the cooler shot. The systematic uncertainty in the measured temperature, $u_{T_{optical}}$, from applying Equation 15 to the raw data is found by considering the propagation of error as in [40–42]. The derivatives in

$$u_{T_{optical}} = \sqrt{\left(u_1 \frac{\partial T_{optical}}{\partial u_1}\right)^2 + ... + \left(u_i \frac{\partial T_{optical}}{\partial u_i}\right)^2} \tag{19}$$

cannot be found analytically and are approximated by the finite difference method. Equation 15 is not linear with temperature, so to bound the error, the largest derivative of $T_{Optical}$ with respect to each input, u_i, is chosen. The largest sources of uncertainty are identified as: the optical transmission correction F_G, the amount of seeded lithium N_0, the solid angle Ω, the probe volume V, the $\mathbf{A_{i1}}$ coefficients, the quenching rates $\mathbf{Q_{i1}}$, and the vibrational relaxation time, τ_{N_2}. These (Table 3) uncertainties are estimated to a 95% confidence interval.

Input	N_0	V	Ω	F_G	$\mathbf{A_{i1}}$	$\mathbf{Q_{i1}}$	τ_{N_2}
Uncertainty ($\%$)	30	20	10	5	10	25	50

Table 3: Estimates of the systemic uncertainty in the input parameters for Equation 15

The uncertainty in the amount of seeded lithium, N_0, is based upon inspection of the raw traces of the photodetector. The probe volume uncertainty, V, is an estimate based on ray tracing and the numerical aperture of the fiber. Estimation of the uncertainty in the calculation of the solid angle, Ω, is from the measurements of optical layout. Uncertainty in the non-ideal glass correction, F_G, is estimated by inspecting the appropriate commercial vendor's specification sheet. Uncertainty in $\mathbf{A_{i1}}$ is estimated by conservatively reviewing the data in [21, 22]. The uncertainty in the calculation of $\mathbf{Q_{i1}}$ is determined by reviewing the data in [24–26] and how the constants used from these data are applied to calculations involving the flow in T5. The uncertainty in the vibrational relaxation time of N_2 is the most difficult to bound. The uncertainty in τ_{N_2} is found by inspecting the data and results presented in [27, 28, 32, 33]. Particularly, p. 197 of [27] describes the relaxation time of N_2 as extremely sensitive to impurities; for example, a 2% water vapor mixture is found to change the relaxation time by a factor of 2. The seeded lithium may act as an impurity, albeit the concentration is low ($\sim 0.3\%$ by mass). The uncertainty in τ_{N_2} is estimated by inspecting the data in the literature. Combining all of the uncertainties (Table 3) as in Equation 19 leads to an uncertainty of 12% in the magnitude of $T_{Optical}$ with a 95% confidence interval. This estimation of systematic uncertainty appears as error bars in Figure 6.

4.0 LASER DIFFERENTIAL INTERFEROMETRY

Laser differential interferometry (reviewed in [43, 44]) is an appropriate technique for use in T5 for a number of reasons, but primarily because it is (relative to the schlieren technique) insensitive to mechanical vibrations and (relative to the shadowgraph technique) highly sensitive. The optical setup (Figure 7) is arranged such that the finite fringes are oriented at 45 degree angles to the cone; this orientation results in the examination of density

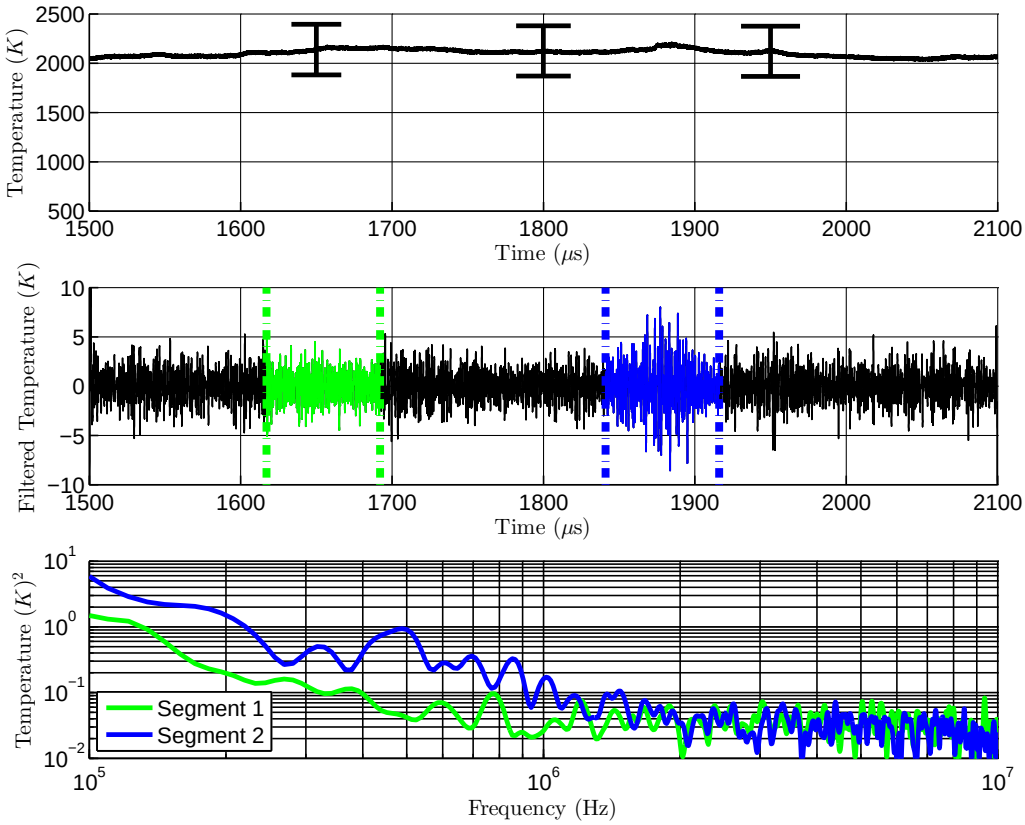

Figure 6: From top to bottom: Raw, Filtered and Spectral Response of the detection technique during shot 2668 (details of conditions found in Table 2). In the top plot, the raw response is plotted to show the near constant irradiance on the photodetector. The response fluctuates with time, standard deviation of 36 K during the run time. The raw response is band-pass filtered and presented in the middle plot to accentuate the periods of fluctuation. On the bottom, the power spectral density (Welch Method, Δf = 50 kHz), Overlap - 50 $\%$) of color coded time windows.

gradients both normal and parallel to the surface of the cone.

A high-speed camera (76k FPS, 800×104 pixels) is placed in the image plane for shot 2672 ($h_R = 10.6$ MJ/kg, $p_R = 49$ MPa). Selected images from the experiment (Figure 8) are processed to improve contrast (each image is subtracted from the RMS image) and show transitional features passing through the field of view. For clarity, the flow is from left to right, the cone's surface is marked by a white line, and a 1 mm length-scale and time-stamp are provided. At first glance it appears that there is a length scale associated with the disturbance, but this is merely the difference in sensitivity throughout fringe space in a finite fringe differential interferogram. The surface mounted thermocouples do not register any significant deviation from the predicted laminar heat-flux level at the imaged location, indicating that the imaged phenomena are turbulence precursors, rather than turbulent spots of high intensity. This is encouraging, and a more sensitive device based on the principles described in [45–47] is being designed at the time of this writing.

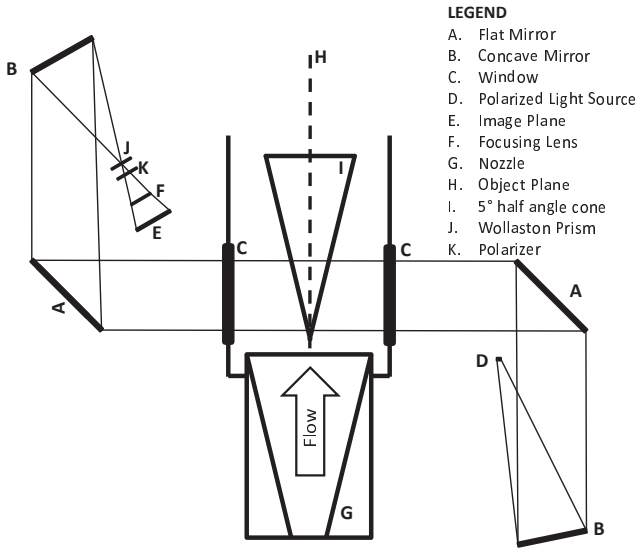

Figure 7: Schematic of the optical setup for Laser Differential Interferometry in T5.

5.0 CONCLUSION

We have identified a need for a high-speed optical detection technique to measure transitional behavior in hypervelocity boundary layers. We have implemented two approaches utilizing optical detection: a point temperature measurement by spontaneous emission and, a two-dimensional imaging technique, laser differential interferometry. A model for the spontaneous emission of a trace gas in the boundary layer is used to quantitatively interpret the detection output. The results indicate that the technique can be used to track turbulent bursts, but cannot track linear wave packets. The systematic error associated with the spontaneous emission technique is large, primarily due to the uncertainty in the amount of Li in the test slug, and the prediction of vibrational relaxation time of N_2. A laser differential interferometric technique is implemented using high-speed video of a segment of the boundary layer. The results of the LDI method are encouraging, demonstrating the ability to track turbulent precursors.

ACKNOWLEDGMENTS

Thanks to Bahram Valiferdowsi for the isometric views of the solid model of the facility and helping run the facility. This work was sponsored by AFOSR/National Center for Hypersonic Research in Laminar-Turbulent Transition, for which Dr. John Schmisseur is the program manager. The views and conclusions contained herein are those of the authors and should not be interpreted as necessarily representing the official policies or endorsements, either expressed or implied, of the Air Force Office of Scientific Research or the U.S. Government.

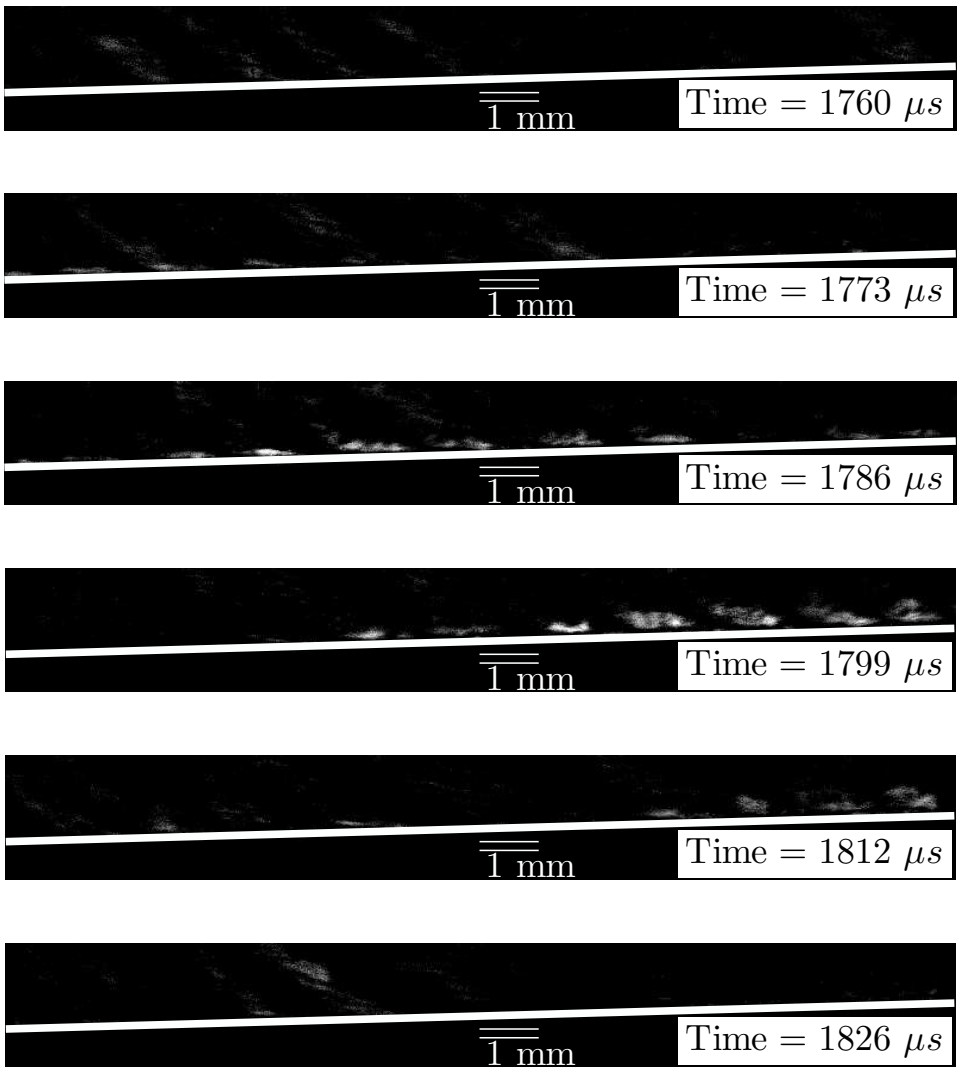

Figure 8: Differential interferograms from Shot 2672 (h_R = 10.6 MJ/kg, p_R = 49MPa). For clarity, the flow is from left to right, the cone's surface is marked by a white line, and a 1 mm length-scale/time-stamp are provided. The finite fringe spacing is approximately 4 mm; this is the apparent faux structure in the boundary layer.

REFERENCES

[1] Mack, L. M., "Linear Stability Theory and the Problem of Supersonic Boundary-Layer Transition," *AIAA*, Vol. 13, No. 13, July 1975, pp. 278–289.

[2] Mack, L. M., "Boundary-Layer Linear Stability Theory," *AGARD Rep 709*, Spec. Course Stab. Transit. Laminar Flows 1984.

[3] Stetson, K. and L., K. R., "On Hypersonic Boundary-Layer Stability," *AIAA*, Presented at AIAA Aerosp. Sci. Meet. Exhib., 30th, Reno 1992.

[4] Federov, A., "Transition and Stability of High-Speed Boundary Layers," *Annu. Rev. Fluid Mech*, Vol. 43, August 2011, pp. 79–95.

[5] Germain, P., "The Boundary Layer on a Sharp Cone in High-Enthalpy Flow," *California Institute of Technology, PhD Thesis*, 1993.

[6] Adam, P., "Enthalpy Effects on Hypervelocity Boundary Layers," *California Institute of Technology, PhD Thesis*, 1997.

[7] Rasheed, A., "Passive Hypervelocity Boundary Layer Control Using an Acoustically Absorptive Surface," *California Institute of Technology, PhD Thesis*, 2001.

[8] Fujii, K. and Hornung, H. G., "Experimental Investigation of High-Enthalpy Effects on Attachment-Line Boundary-Layer Transition," *AIAA*, Vol. 41, No. 7, July 2003, pp. 1282–1291.

[9] Casper, K. M., "Hypersonic Wind-Tunnel Measurements of Boundary-Layer Pressure Fluctuations," *Purdue University, Master's Thesis*, 2011.

[10] Heitmann, D., Kähler, C., Radespiel, R., Rodiger, T., Knauss, H., and Wagner, S., "Non-Intrusive Generation of Instability Waves in a Planar Hypersonic Boundary Layer," *Experiments in Fluids*, Vol. 50, August 2011, pp. 457–464.

[11] Johnson, H. B., Seipp, T. G., and Candler, G. V., "Numerical Study of Hypersonic Reacting Boundary Layer Transition on Cones," *Physics of Fluids*, Vol. 10, No. 13, October 1998, pp. 2676–2685.

[12] Miles, R. B., "Resonant Doppler Velocimeter," *Physics of Fluids*, Vol. 18, No. 6, 1975, pp. 751–752.

[13] Zimmermann, M. and Miles, R. B., "Hypersonic-Helium-Flow-Field Measurements with the Resonant Doppler Velocimeter," *Applied Physics Letters*, Vol. 37, No. 10, 1980, pp. 885–887.

[14] Cheng, S., Zimmermann, M., and Miles, R. B., "Supersonic-Nitrogen Flow-Field Measurements with the Resonant Doppler Velocimeter," *Applied Physics Letters*, Vol. 43, No. 2, 1983, pp. 143–145.

[15] Cheng, S., Zimmermann, M., and Miles, R. B., "Separation of Time-Averaged Turbulence Components by Laser-Induced Fluorescence," *Physics of Fluids*, Vol. 26, No. 4, 1983, pp. 874–877.

[16] Seitzman, J. M., Kychakoff, G., and Hanson, R. K., "Instantaneous Temperature Field Measurements Using Planar Laser-Induced Fluorescence," *Optical Letters*, Vol. 10, No. 9, Sep 1985, pp. 439–441.

[17] Eckbreth, A. C., *Laser Diagnostics for Combustion Temperature and Species*, Gordon and Breach Publications, 2nd ed., 1996.

[18] Herzberg, G., *Atomic Spectra and Atomic Structure*, Dover Publications, 2nd ed., 1944.

[19] McQuarrie, D., *Statistical Mechanics*, University Science Books, 2000.

[20] *National Institute of Standards and Technology; Physical Measurement Laboratory: NIST Atomic Spectra Database*.

[21] Gaupp, A., Kuske, P., and Andrä, H. J., "Accurate Lifetime Measurements of the Lowest $^2P_{1/2}$ States in Neutral Lithium and Sodium," *Phys. Rev. A*, Vol. 26, Dec 1982, pp. 3351–3359.

[22] Yan, Z.-C. and Drake, G. W. F., "Theoretical Lithium $2^2\,S \rightarrow 2^2\,P$ and $2^2\,P \rightarrow 3^2\,D$ Oscillator Strengths," *Phys. Rev. A*, Vol. 52, Dec 1995, pp. R4316–R4319.

[23] Crosley, D. R., "Semiquantitative Laser-induced Fluorescence in Flames," *Combustion and Flame*, Vol. 78, No. 1, 1989, pp. 153 – 167, Special issue on the Ein Gedi Workshop on Combustion.

[24] Jenkins, D. R., "The Determination of Cross-Sections for the Quenching of Resonance Radiation of Metal Atoms. IV. Results for Lithium," *Proceedings of the Royal Society of London. Series A, Mathematical and Physical Sciences*, Vol. 306, No. 1486, September 1968, pp. 413–421.

[25] Fisher, E. R. and Smith, G. K., "Vibration-Electronic Coupling in the Quenching of Electronically Excited Alkali Atoms by Diatomics," *Applied Optics*, Vol. 10, No. 8, Aug 1971, pp. 1803–1813.

[26] Fisher, E. and Smith, G., "Alkali Quenching in High Temperature environments," *Chemical Physics Letters*, Vol. 13, No. 5, 1972, pp. 448 – 452.

[27] Gaydon, A. G. and Hurle, I. R., *The Shock Tube in High-Temperature Chemical Physics*, Reinhold Publishing Corporation, 1st ed., 1963.

[28] Hurle, I. R., "Line-Reversal Studies of the Sodium Excitation Process Behind Shock Waves in N_2," *The Journal of Chemical Physics*, Vol. 41, No. 12, 1964, pp. 3911 – 3920.

[29] Park, C., *Nonequilibrium Hypersonic Aerothermodynamics*, John Wiley & Sons, 1st ed., 1990.

[30] Fisher, E. R. and Smith, G. K., "Vibrational Relaxation by Metal Atoms," *Chemical Physics Letters*, Vol. 6, No. 5, 1970, pp. 438 – 440.

[31] Eremin, A., Kulikovsky, A., and Naboko, I., "Sodium Excitation in Non-equilibrium Conditions Behind Shock Waves in Nitrogen," *Chemical Physics Letters*, Vol. 45, No. 2, 1977, pp. 351 – 355.

[32] Blackman, V., "Vibrational Relaxation in Oxygen and Nitrogen," *Journal of Fluid Mechanics*, Vol. 1, No. 01, 1956, pp. 61–85.

[33] Vincenti and Kruger, *Introduction to Physical Gas Dynamics*, Krieger Publishing Company, 1965.

[34] Hirschel, E. H. H., *Basics of Aerothermodynamics*, Springer-Verlag Berlin Heidelberg, 2005.

[35] Mcintosh, M. K., "A Computer Program for the Numerical Calculation of Equilibrium and Perfect Gas Cnditions in Shock Tunnels," Technical Report CPD 169, Australian Defense Scientific Service, 1969.

[36] Lordi, J., Mates, R. E., and Moselle, J. R., "Computer Program for the Numerical Solution of Nonequilibrium Expansions of Reacting Gas Mixtures," NASA CR-472, 1966.

[37] Lees, L., "Laminar Heat Transfer over Blunt-Nosed Bodies at Hypersonic Flight Speeds," *Jet Propulsion*, 1956.

[38] White, F., *Viscous Fluid Flow*, McGraw-Hill, 2nd ed., 1991.

[39] Jocksch, A. and Kleiser, L., "Growth of Turbulent Spots in High-speed Boundary Layers on a Flat Plate," *International Journal of Heat and Fluid Flow*, Vol. 29, No. 6, 2008, pp. 1543 – 1557.

[40] Kline, S. J. and McClintock, F. A., "Describing Uncertainties in Single Sample Experiments," *Mechanical Engineering*, Vol. 75, 1953, pp. 3–8.

[41] Moffat, R. J., "Describing the Uncertainties in Experimental Results," *Experimental Thermal and Fluid Science*, Vol. 1, No. 1, 1988, pp. 3–17.

[42] Beckwith, T. G., Marangoni, R. D., and Lienhard, J. H., *Mechanical Measurments*, Pearson-Prentice Hall, Sixth ed., 2007.

[43] Merzkirch, W., *Flow Visualization*, Academic Press, 1974.

[44] Settles, G. S., *Schlieren and Shadowgraph Techniques*, Springer-Verlag Berlin Heidelberg, 1st ed., 2001.

[45] Salyer, T. R., Collicott, S. H., and Schneider, S. P., "Feedback Stabilized Laser Differential Interferometry for Supersonic Blunt Body Experiments," *AIAA*, Presented at AIAA Aerosp. Sci. Meet. Exhib., 38th, Reno 2000.

[46] Smeets, G. and Goerge, A., "Gas Dynamic Investigations in a Shock Tube using a Highly Sensitive Interferometer," *Translation of ISL Internal Report 14/71*, Original 1971, Translation 1996.

[47] Smeets, G. and Goerge, A., "Laser Differential Interferometer Applications in Gas Dynamics," *Translation of ISL Internal Report 28/73*, Original 1975, Translation 1996.